ADVANCED ELECTRONIC MATERIALS Open Access
www.advelectronicmat.de

Ag Nanowire-Integrated MoS_2/ZnO Heterojunctions for Highly Efficient Photogenerated Charge Transfer

Anh Thi Nguyen, Jungyoon Cho, Malkeshkumar Patel, Duc Anh Vu, Jungeun Song, Dongseok Suh, Ambrose Seo, Joondong Kim, and Dong-Wook Kim**

The integration of silver nanowire (AgNW) networks with MoS_2/ZnO heterojunctions leads to a remarkable enhancement in surface photovoltage (SPV) response. In the visible wavelength range, the heterojunctions with AgNWs achieve an SPV signal of ≈200 mV, a fourfold increase compared to the counterparts without AgNWs (≈50 mV). Wavelength-dependent nanoscopic SPV mapping suggests that this enhancement originates from efficient charge transfer between MoS_2 and ZnO. Moreover, the embedded AgNWs raise the local electric potential at the MoS_2 surface by several tens of mV, thereby facilitating the collection of photogenerated electrons. Optical calculations reveal that AgNWs concentrate incident light in neighboring layers across a broad wavelength range, further boosting photocarrier generation. These results, along with photoluminescence spectra, suggest that photocarrier transfer at the MoS_2/ZnO heterointerfaces is significantly enhanced due to the synergistic effects of light concentration, local potential modifications, and improved electric conduction caused by the AgNW networks.

1. Introduction

The intriguing physical properties of transition metal dichalcogenides (TMDs), including their huge exciton binding energies,[1–3] sizable bandgaps,[1–7] and high electron mobility[1,4] have attracted considerable research attention. To fully exploit these remarkable features for functional devices, the fabrication of TMD-based heterostructures, analogous to those found in conventional 3D semiconductor materials, is crucial.[8–18] While heterostructures exclusively composed of 2D materials have been extensively investigated, integrating 2D and 3D materials offers a more versatile pathway toward the development of high-performance devices.[11–18] This strategy leverages the well-established fabrication techniques of 3D materials and the comprehensive understanding of 3D device mechanisms. Furthermore, emergent physical phenomena can appear in multi-dimensional heterojunctions due to improved light-matter interaction, strong electronic interaction, and elastic strain, thereby enriching the scope of potential applications.[11–16]

The combination of TMDs and wide-bandgap oxide semiconductors (WOS) has been investigated to develop 2D-3D heterostructure-based optoelectronic devices.[11–18] The large bandgap of WOS leads to the formation of a type II band alignment at the TMD/WOS interface, promoting efficient electron transfer from TMD to WOS and hole transfer in the opposite direction.[12–16] This spatial separation of charge carriers enables their efficient collection prior to recombination. Such charge transfer capabilities are advantageous for applications in catalysts[12] and photodetection.[15,16] Among WOS materials, ZnO is one of the most widely utilized due to its superior material properties and well-established growth techniques.[14–21] In TMD/ZnO heterojunctions, further improvement of interfacial charge transfer is essential for achieving high quantum efficiency, which quantifies the fraction of incident photons converted into collected charges.[13,16]

Silver nanowire (AgNW) networks have been widely used as transparent electrodes due to their low sheet resistance, outstanding optical transmittance, mechanical flexibility, and easy fabrication processes.[22–24] These unique features make AgNWs ideal

A. T. Nguyen, J. Cho, J. Song, D. Suh, A. Seo, D.-W. Kim
Department of Physics
Ewha Womans University
Seoul 03760, South Korea
E-mail: dwkim@ewha.ac.kr
M. Patel, J. Kim
Department of Electrical Engineering
Incheon National University
Incheon 22012, South Korea
E-mail: joonkim@inu.ac.kr
D. A. Vu
Department of Energy Science
Sungkyunkwan University
Suwon 16419, South Korea
A. Seo
Department of Physics and Astronomy
University of Kentucky
Lexington, KY 40506, USA

The ORCID identification number(s) for the author(s) of this article can be found under https://doi.org/10.1002/aelm.202400744

© 2025 The Author(s). Advanced Electronic Materials published by Wiley-VCH GmbH. This is an open access article under the terms of the Creative Commons Attribution License, which permits use, distribution and reproduction in any medium, provided the original work is properly cited.

DOI: 10.1002/aelm.202400744

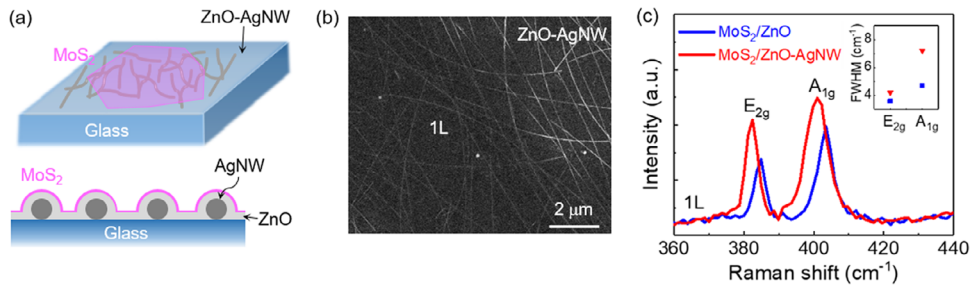


Figure 1. a) Schematic diagrams of a MoS_2/ZnO-AgNW heterojunction. The lower diagram illustrates a simplified cross-section view of the heterojunction structure. b) Scanning electron microscope image of a MoS_2/ZnO-AgNW heterojunction sample. The labels "1L" and "ZnO-AgNW" indicate the MoS_2 monolayer flake and the bare ZnO-AgNW layer, respectively. The ZnO-AgNW region covered by the MoS_2 monolayer appears darker compared to the uncovered region. c) Raman spectra of 1L-MoS_2/ZnO-AgNW (red) and 1L-MoS_2/ZnO (blue). The $E_{2\ g}$ and $A_{1\ g}$ peaks of 1L-MoS_2/ZnO-AgNW are more intense and shifted to lower energies compared to those of 1L-MoS_2/ZnO. In addition, 1L-MoS_2/ZnO-AgNW exhibits broader peak widths than 1L-MoS_2/ZnO.

for use in various transparent optoelectronic devices, including flexible displays,[23] light-emitting diodes (LEDs),[23] photovoltaic devices,[21,24] and smart windows.[23] Additionally, surface plasmon excitation in AgNWs can boost the creation of photogenerated charge carriers in adjacent semiconductor layers.[21,24] Despite these benefits, the repetitive operation of AgNW-containing devices often results in Joule heating, which may cause thermal damage and degrade overall device performance.[22,23] To mitigate this, AgNWs passivated with ZnO thin films (ZnO-AgNW) have exhibited improved long-term stability.[21,23,24] By leveraging the promising attributes of AgNWs, the fabrication of TMD/ZnO-AgNW heterojunctions and investigation of their charge transfer characteristics can provide an attractive approach for developing advanced TMD/WOS heterostructures.

Transparent and conducting AgNW networks, composed of AgNWs with lengths of ≈10 microns, exhibit excellent electrical conductivity and optical transparency.[21–24] Consequently, the fabrication of TMD/ZnO-AgNW heterojunctions requires a reliable method to produce large-area TMD layers. However, conventional tape-based mechanical exfoliation techniques are limited, typically yielding TMD flakes only several microns in size.[8] To overcome this constraint, metal-assisted exfoliation (MAE) has emerged as an effective alternative. This method exploits strong van der Waals or covalent-like quasi-bonding interactions between metals and TMD layers, enabling the production of large-area, uniform TMD layers.[9–11] Additionally, the MAE technique proves advantageous for the fabrication of vertically stacked TMD heterojunctions, as demonstrated in our previous work.[10] By employing TMD layers exfoliated on insulating substrates (e.g., SiO_2/Si), researchers have fabricated quasi-vertical TMD heterojunctions, where the electric current flows not only perpendicular to the heterointerfaces but also laterally across the thin TMD layers. As a result, vertical heterojunctions mitigate concerns about recombination losses during lateral transport through thin TMD layers.

In this paper, a fabrication procedure for high-quality TMD/ZnO-AgNW heterojunctions is presented. By utilizing the MAE technique, TMD flakes with sizes reaching hundreds of microns are prepared to fully cover AgNW networks. Comparative investigations of MoS_2/ZnO heterojunctions, with and without AgNWs, clearly demonstrate that highly conducting AgNWs enhance broad-band optical absorption and induce electric potential modifications in the MoS_2 layers. Nanoscopic surface potential mappings and careful optical characterizations reveal that AgNWs significantly boost photocarrier transfer at the MoS_2/ZnO heterointerfaces. This work introduces a versatile approach for integrating TMD/ZnO-AgNW heterojunctions and highlights their potential for high-performance optoelectronic devices.

2. Results and Discussion

The schematic diagrams of the heterojunctions – MoS_2 flakes and ZnO-AgNW layers on glass substrates – are illustrated in **Figure 1a**. MoS_2 monolayer flakes, exceeding hundreds of microns in size, are successfully prepared using the MAE method (Figure S1, Supporting Information). The MAE-prepared MoS_2 flakes were subsequently transferred onto ZnO-AgNW layers (Figures S2 and S3, Supporting Information) using polymer films. The ZnO coating improves both the thermal stability and electrical conductivity of the AgNW network (Figure S2, Supporting Information). At a wavelength of 550 nm, the transmittance of the AgNW and ZnO-AgNW samples exceeds 80% (Figure S3a, Supporting Information). Optical characterizations and analyses of ZnO-AgNW confirm that the intrinsic optical properties of the ZnO layers are well-preserved (Figure S3d, Supporting Information). These results demonstrate the outstanding electrical and optical performance of ZnO-AgNW for transparent electrode applications. The detailed fabrication procedures of MoS_2/ZnO-AgNW heterojunctions are provided in Figure S4 (Supporting Information). The scanning electron microscopy (SEM) image in Figure 1b shows the regions near the edge of a monolayer (1L) MoS_2 flake. The transfer of 2D materials onto 3D nanostructures involves complicated processes that often lead to poor reproducibility and the introduction of defects.[15] Cracks or wrinkles, the most frequently found defects in the transferred TMD flakes, are rarely observed at the 1L-MoS_2 surface on the non-flat ZnO-AgNW layer. The MoS_2 region is distinguishable due to contrast differences in the SEM image (Figure 1b) as well as the optical microscope image (Figure S1b, Supporting Information). A recent study reports that the grayscale values of SEM images allow us to determine the number of TMD layers.[25] Therefore, the homogeneous contrast observed on the MoS_2 surface in Figure 1b confirms the uniform thickness of the flake.

© 2025 The Author(s). Advanced Electronic Materials published by Wiley-VCH GmbH

2199160x, 2025, 6, Downloaded from https://advanced.onlinelibrary.wiley.com/doi/10.1002/aelm.202400744 by Ewha Womans University Library, Wiley Online Library on [10/08/2025]. See the Terms and Conditions (https://onlinelibrary.wiley.com/terms-and-conditions) on Wiley Online Library for rules of use; OA articles are governed by the applicable Creative Commons License

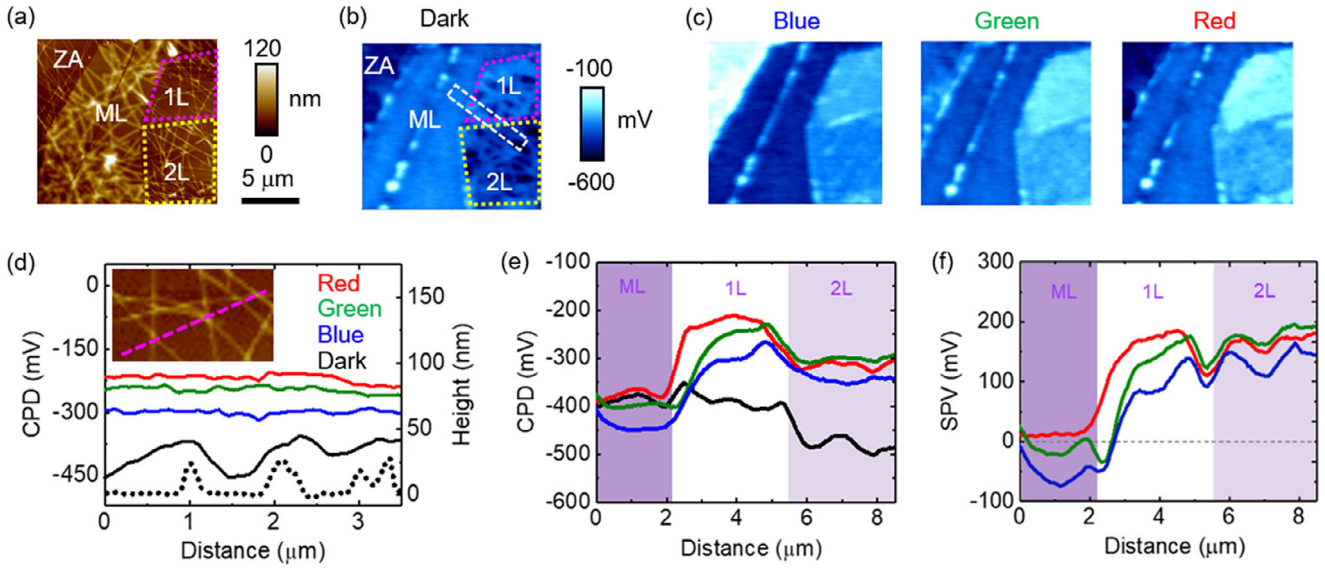


Figure 2. a) AFM image of MoS_2/ZnO-AgNW. The bare ZnO-AgNW surface is labeled as ZA. Regions corresponding to monolayer, bilayer, and multilayer MoS_2 flakes are marked as 1L, 2L, and ML, respectively. b) CPD maps in the dark and c) under the illumination of blue (λ_{peak} = 405 nm), green (λ_{peak} = 522 nm), and red (λ_{peak} = 625 nm) LEDs, with an optical power density of 1.3 mW cm^{-2}. d) CPD profiles (solid lines) and a height profile (black dotted line) of 1L-MoS_2/ZnO-AgNW along the pink-dashed line shown in the inset AFM image. e) CPD and f) SPV profiles obtained by averaging the values in the white-dashed rectangle in (b).

Figure 1c shows micro-Raman spectra of the heterostructures without (MoS_2/ZnO) and with embedded AgNW networks (MoS_2/ZnO-AgNW). For MoS_2/ZnO, the in-plane $E_{2\ g}$ and out-of-plane $A_{1\ g}$ vibration modes of 1L-MoS_2 exhibit peaks at 385 and 404 cm^{-1}, respectively. For MoS_2/ZnO-AgNW, the $E_{2\ g}$ and $A_{1\ g}$ peaks appear at 383 and 401 cm^{-1}, respectively. The spacings between the $E_{2\ g}$ and $A_{1\ g}$ peaks for the 1L-MoS_2 flakes are 19 and 18 cm^{-1}, comparable to those reported in the literature.[4–6] The notable thickness-dependence of the peak spacing allows the identification of the flake thickness in our heterostructures (Figure S5, Supporting Information).[5]

For 1L-MoS_2, the Raman peak positions depend on the doping concentration as well as the mechanical strain.[4–6] Compared with 1L-MoS_2/ZnO, both $E_{2\ g}$ and $A_{1\ g}$ mode frequencies of 1L-MoS_2/ZnO-AgNW decrease. This suggests that the MoS_2/ZnO-AgNW heterostructures undergo tensile strain and electron doping. The non-flat surface of the ZnO-AgNW layer containing 20-nm-diameter AgNWs can impose strain on the MoS_2 flakes, resulting in non-uniform strain distributions in the MoS_2 flake. The $E_{2\ g}$ peak shift is reported to be −1.7 cm^{-1} per % strain,[5,6] and hence the tensile strain in our 1L-MoS_2/ZnO-AgNW is estimated to be 1.3%. The tensile strain narrows the bandgap energy of MoS_2, with a 1.3% of strain corresponding to a bandgap decrease of 40 meV.[5,6] The AgNW-induced strain can modulate the electric potential distributions at the MoS_2 flake surface, leading to exciton dissociation and subsequent drift of electrons and holes. These effects result in light-induced inhomogeneous doping in the MoS_2 flake. The full-width half-maximum of the $E_{2\ g}$ and $A_{1\ g}$ modes for 1L-MoS_2/ZnO-AgNW are measured to be 4.2 and 7.2 cm^{-1}, respectively, which are larger than those of the $E_{2\ g}$ (3.6 cm^{-1}) and $A_{1\ g}$ (4.7 cm^{-1}) modes for 1L-MoS_2/ZnO, as shown in the inset of Figure 1c. Such broadening and overall redshift of the Raman peaks suggest that the AgNW networks contribute to inhomogeneous strain and electron doping in the MoS_2 flake on the ZnO-AgNW layer.

In order to study the light-induced charge transfer (CT) processes, the AFM and KPFM measurements of the MoS_2/ZnO-AgNW samples were performed, as shown in **Figure 2**a–f. KPFM allows us to directly investigate the interfacial CT processes of heterostructures.[26,27] In particular, the high spatial resolution of KPFM, reaching a few tens of nanometers, enables us to visualize the local CT characteristics in TMD-based nanostructures.[11,15] The AFM image was obtained near the edge of the MoS_2 flake, where the bare ZnO-AgNW, along with 1L, bilayer (2L), and multilayer (ML) MoS_2 regions, are present. Given the large diameter of a single AgNW (≈20 nm), determining the exact number of layers in the ML region from the AFM height profile is practically impossible. Based on the optical contrast, the ML flake is inferred to contain several layers of MoS_2. The randomly oriented AgNWs increase the height of the MoS_2 surface, even in the ML region. In particular, the peak-to-valley height in the 1L MoS_2 region is almost the same as the diameter of the AgNW (Figure 2d). These results suggest that the surface morphology of the flake follows the underlying ZnO-AgNW surface, as illustrated in Figure 1a, ensuring the strain imposed on the MoS_2 flakes in MoS_2/ZnO-AgNW.

The contact potential difference (CPD) maps, obtained using KPFM, are shown in Figure 2b,c. The ZnO-AgNW (ZA), 1L, 2L, and ML regions exhibit distinct contrasts in the dark-state CPD (CPD_D) map (Figure 2b). The mean CPD_D values for the 1L, 2L, and ML regions are measured to be −405, −440, and −380 mV, respectively. The CPD_D difference between the 1L and ML regions is consistent with those reported in the literature.[28] The thickness-dependent variation in CPD_D arises from changes in the band structure and the electron affinity of MoS_2.[1,2] Additionally, the thickness-dependent CPD_D is at-

© 2025 The Author(s). Advanced Electronic Materials published by Wiley-VCH GmbH

2199160x, 2025, 6, Downloaded from https://advanced.onlinelibrary.wiley.com/doi/10.1002/aelm.202400744 by Ewha Womans University Library, Wiley Online Library on [10/08/2025]. See the Terms and Conditions (https://onlinelibrary.wiley.com/terms-and-conditions) on Wiley Online Library for rules of use; OA articles are governed by the applicable Creative Commons License

tributed to the electrostatic screening effect in the MoS_2 layers.[28] The MoS_2/ZnO heterostructures exhibit the type II staggered band alignment; hence, electrons and holes tend to move in opposite directions.[14–18] This spatial separation of electron–hole pairs generates a built-in electric field at the MoS_2/ZnO interface.

Figure 2c shows the CPD maps when illuminated by LEDs with different peak wavelengths, λ_{peak}: blue (λ_{peak}: 405 nm, bandwidth: 13 nm – M405L2, Thorlabs), green (λ_{peak}: 522 nm, bandwidth: 35 nm – M530L4, Thorlabs), and red (λ_{peak}: 625 nm, bandwidth: 16 nm – M617L5, Thorlabs). The beam spot was consistently positioned on the sample for each LED since the fiber-coupled LED light was sent to the sample using an identical focusing lens. All CPD data collected under illumination (CPD_L) were obtained with an optical power density of 1.3 mW cm^{-2}. Prior to the measurement using a next light source, the sample was kept in the dark for sufficient time to allow the measured CPD_D to return to its initial value. This procedure ensures that the data obtained with each LED are not affected by previous illuminations.

Figure 2d shows the height and CPD profiles of 1L-MoS_2/ZnO-AgNW along the pink-dashed line in the inset AFM image. The comparison of the topography and CPD_D reveals that the underlying AgNWs increase the local electric potential (i.e., CPD_D) at the MoS_2 surface. The AgNW-induced strain in the MoS_2 flakes modulates the electric potential distributions at the surface. Upon light exposure, the measured CPD increases, with significant light-induced CPD changes observed under green and red LED illumination. The optical absorption coefficients of 1L-MoS_2 are very high ($\approx 10^6$ cm^{-1}) at the peak wavelengths of these LEDs,[3] resulting in the generation of a large number of excitons in MoS_2. The type II band alignment at the MoS_2/ZnO interface separates the photogenerated excitons and enables the transfer of electrons from MoS_2 to ZnO.[14–18] Consequently, the accumulation of the remaining holes leads to positive charging at the MoS_2 surface, thereby increasing the surface electric potential as reflected in the light-induced CPD changes.

Figure 2e shows the CPD profiles acquired from the white-dashed border rectangle region in Figure 2b, containing the 1L, 2L, and ML regions. The light exposure increases the measured CPD; in particular, large increases are observed in the 1L and 2L regions. Figure 2f shows the profiles of surface photovoltage (SPV), defined as $CPD_L - CPD_D$, derived from the CPD profiles in Figure 2e. Large positive SPV signals, reaching almost 200 mV, are observed in the 1L and 2L regions of MoS_2/ZnO-AgNW. For comparison, multiple 1L areas on the identical sample were selected, and CPD data were acquired from these areas (Figure S6, Supporting Information). The CPD measurements across all 1L areas were consistent, confirming the high uniformity of the sample fabrication process. Additionally, during the CPD measurements, the entire sample surface was exposed to light. The consistency in the measured CPD results indicates no evidence of sample degradation. When exposed to light, the ML region exhibits a little change in CPD (red LED) and even a drop in CPD (blue and green LEDs), as shown in Figure 2e,f. Such thickness dependence indicates that the CT processes at the MoS_2/ZnO interface dominantly influence the light-induced CPD changes. The local potential at the top surface of the MoS_2/ZnO-AgNW heterostructure is strongly influenced by the electrical contact at the MoS_2/ZnO interface. For example, variations in the gap between the MoS_2 flakes and the underlying ZnO-AgNW layers could lead to substantial differences in interfacial charge transfer characteristics and, consequently, in light-induced CPD changes. However, the measured CPD data, primarily determined by the layer thickness as shown in Figure 2b–f, indicate that our MoS_2/ZnO-AgNW heterostructure exhibits homogeneous interfacial contacts.

The SPV characteristics of MoS_2/ZnO are also investigated, as shown in **Figure 3**a–e. Not only the bare ZnO surface but also the MoS_2 regions with different thicknesses can be identified due to the contrast in the dark-state CPD map (Figure 3b). When exposed to light, each region exhibits light-induced CPD changes, as shown in Figure 3c. At the bare ZnO surface, the measured SPV values are nearly zero under green and red LED illumination (Figure 3d). Under blue LED illumination, the bare ZnO layer exhibits positive SPV signals up to 50 mV. The photons from blue LED have smaller energy than the bandgap energy of ZnO (3.2 eV).[14–18] Thus, the non-zero SPV signals under blue LED illumination indicate the contribution of defect states in ZnO (represented by the red bars in Figure 3e).[27,29] The upward band bending occurs at the n-type semiconductor ZnO surface,[26,27] and hence the valence band holes migrate toward the surface, resulting in positive SPV signals. Furthermore, the SPV measurements of MoS_2 flakes transferred onto AgNW/glass substrates (Figure S7, Supporting Information) reveal that the SPV signal at 522 nm for MoS_2/AgNW is only 50 mV – significantly lower than that for MoS_2/ZnO-AgNW. These comparative studies clearly indicate that embedding AgNWs into ZnO layers enhances the photogenerated charge transfer at the MoS_2/ZnO heterointerface.

The type-II band alignment at the MoS_2/ZnO interface is expected,[14,15] as illustrated in the band diagrams in Figure 3e. When illuminated with green and red LEDs, MoS_2/ZnO exhibits positive SPV signals (Figure 3d), attributed to electron transfer from MoS_2 to ZnO. The measured SPV signals for MoS_2/ZnO are below 50 mV, almost 1/4 of those for MoS_2/ZnO-AgNW (Figure 2f). This comparison clearly reveals suppressed CT processes at the MoS_2/ZnO heterointerface. Interestingly, exposure to blue LED light on the MoS_2/ZnO heterojunction results in negative SPV signals of −100 mV (Figure 3d), indicating negative charging at the surface.[26] Thin MoS_2 flakes with only a few layers cannot absorb all the incident photons.[3] As mentioned above, visible light photons can excite electrons to the defect states in the ZnO layer.[27,29] The following scenario can explain the observed negative SPV: Trapped electrons within the ZnO layer inhibit electron transfer from MoS_2 to ZnO, while holes in the valence band migrate away from the surface through diffusion.[27] The middle and right band diagrams of Figure 3e illustrate the suggested charge redistribution behaviors under long-wavelength and short-wavelength light illumination, respectively.

The SPV characteristics of a bare ZnO-AgNW sample provide further insights into the wavelength-dependent SPV behaviors of the MoS_2/ZnO-AgNW heterojunction. As expected, SPV signals at the ZnO-AgNW surface were nearly zero under illumination with red LED (Figure S8a,b, Supporting Information). However, under blue and green LED illumination, positive SPV signals of 300 and 50 mV, respectively, were observed at the ZnO-AgNW surface. Sub-bandgap photons from green and blue LEDs can excite electrons to the defect states in the ZnO layer.[27,29]

© 2025 The Author(s). Advanced Electronic Materials published by Wiley-VCH GmbH

2199160x, 2025, 6, Downloaded from https://advanced.onlinelibrary.wiley.com/doi/10.1002/aelm.202400744 by Ewha Womans University Library, Wiley Online Library on [10/08/2025]. See the Terms and Conditions (https://onlinelibrary.wiley.com/terms-and-conditions) on Wiley Online Library for rules of use; OA articles are governed by the applicable Creative Commons License

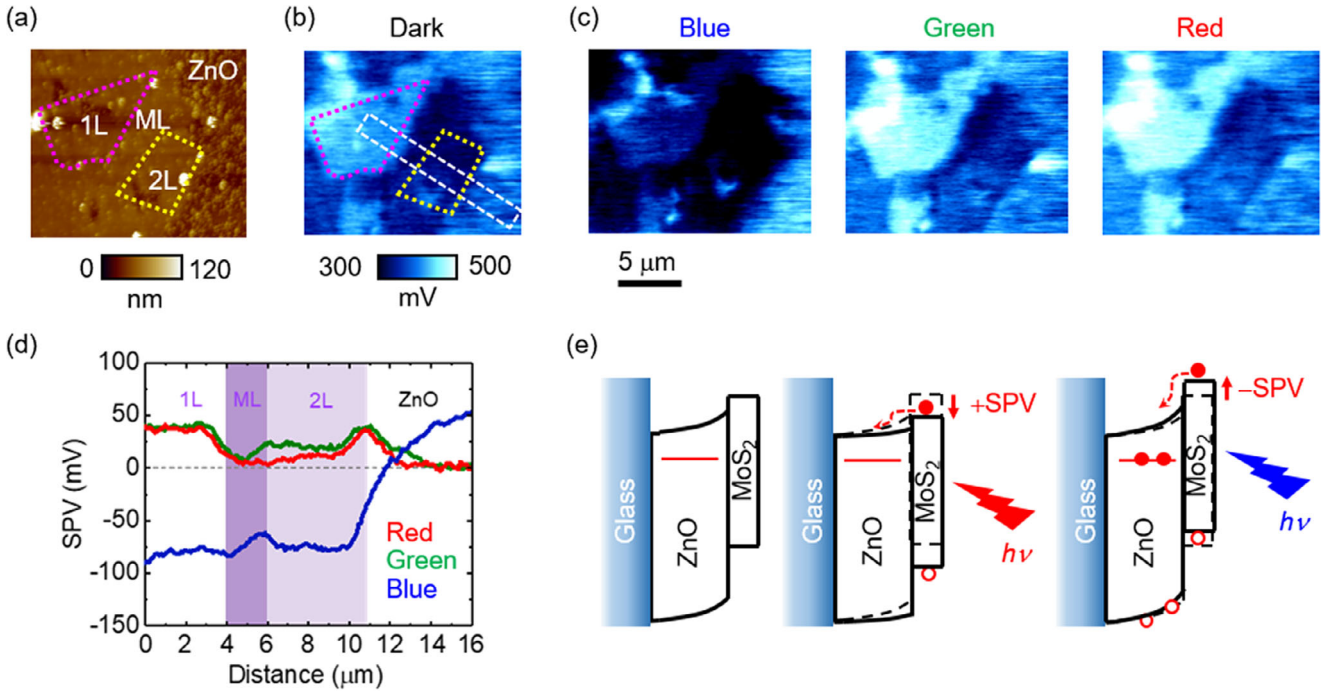


Figure 3. a) AFM image of MoS_2/ZnO. Regions corresponding to the bare ZnO surface are labeled as ZnO. b) CPD maps in the dark and c) under the illumination of blue (λ_{peak} = 405 nm), green (λ_{peak} = 522 nm), and red (λ_{peak} = 625 nm) LEDs, with an optical power density of 1.3 mW cm^{-2}. d) SPV profiles, averaged from the values within the white-dashed rectangle in (b). e) Schematic band diagrams of 1L-MoS_2/ZnO in the dark (left), exposed to long-wavelength light (middle), and exposed to short-wavelength light (right). The red bars in the ZnO layers denote defect states, which can trap photogenerated electrons, as illustrated.

The trapped electrons in the defect states can be transferred to the grounded AgNW networks (Figure S8c, Supporting Information). Consequently, the large positive SPV signals at the ZnO-AgNW surface can appear under blue LED illumination. The wavelength-dependent SPV behaviors of the bare ZnO-AgNW sample indicate an efficient charge collection capability of the AgNW networks.

The electric field intensity distributions in the cross-section of ZnO-AgNW under the illumination of light with wavelengths of 405, 530, and 625 nm obtained by the FDTD calculations are shown in **Figure 4**. For simplicity, a periodic array of AgNWs with a diameter of 20 nm and a period of 1 μm, conformally coated with 15-nm-thick ZnO films, was considered in the calculations. The incident light is linearly polarized perpendicular to the AgNW axes. An intensively localized field is observed inside the AgNWs under the illumination of 405 nm light. This suggests that the localized surface plasmon resonance occurs at a wavelength of ≈400 nm.[21,24] The measured optical reflectance spectra of ZnO-AgNW samples exhibit broad dips near 400 nm (Figure S3b, Supporting Information), indicating the AgNW-induced LSP resonance. When the electric field of the incident light is perpendicular to the AgNW axis, the LSP mode appears in the visible region.[30] This generates a concentrated electric field that appears around the AgNWs, extending across a broad wavelength range beyond the resonance wavelength. As a result, the AgNW networks exhibit significant light scattering and affect the optical properties of the MoS_2 flakes in the MoS_2/ZnO-AgNW heterojunctions. Figure 1c shows that the ZnO-AgNW layer increases the Raman intensity of the MoS_2 flakes, which can be attributed to the improved absorption caused by the concentrated electric field around the AgNWs.

Figure 5a–c illustrate the schematic band diagrams of 1L-MoS_2/ZnO-AgNW in the dark and under light illumination. The conduction band minimum of ZnO is known to be very close to

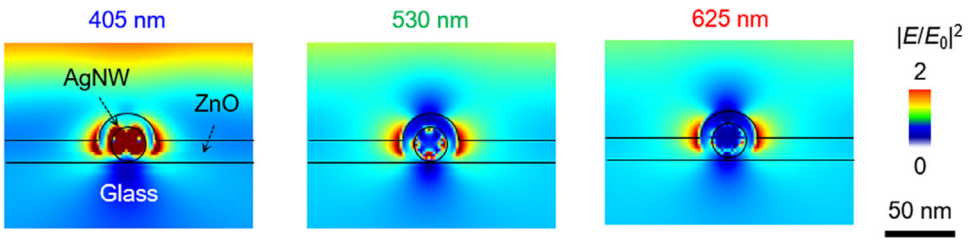


Figure 4. FDTD-calculated electric field (E) intensity distributions of ZnO-AgNW under the illumination of light polarized perpendicular to the AgNW axis. Wavelengths of 405, 530, and 625 nm are used at a normal incidence angle. E_0 represents the electric field magnitude of the incident light.

© 2025 The Author(s). Advanced Electronic Materials published by Wiley-VCH GmbH

2199160x, 2025, 6, Downloaded from https://advanced.onlinelibrary.wiley.com/doi/10.1002/aelm.202400744 by Ewha Womans University Library, Wiley Online Library on [10/08/2025]. See the Terms and Conditions (https://onlinelibrary.wiley.com/terms-and-conditions) on Wiley Online Library for rules of use; OA articles are governed by the applicable Creative Commons License

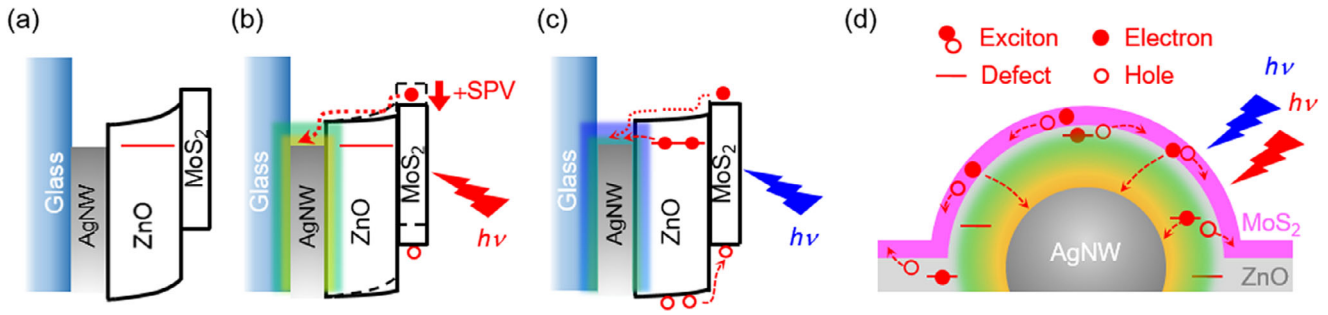


Figure 5. Schematic band diagrams of 1L-MoS_2/ZnO-AgNW: a) in the dark, b) exposed to long-wavelength light, and c) exposed to short-wavelength light. The red bars in the ZnO layers denote defect states, which can trap photogenerated electrons, as illustrated in (c). d) A cross-sectional schematic diagram illustrating the photogenerated excitons and charge carriers in 1L-MoS_2/ZnO-AgNW. Defect states in ZnO, trapping electrons, are indicated as red bars in (a–c).

the Fermi level of Ag, forming a low Schottky barrier contact.[29,31] This enables efficient charge transfer at the ZnO/AgNW interface. Due to the type-II band alignment, the photogenerated electrons in MoS_2 can be transferred to ZnO, while the holes remain in MoS_2. In MoS_2/ZnO-AgNW, the highly conducting AgNWs under the ZnO layers will collect the transferred electrons. The resulting charge redistribution results in positive SPV signals exceeding 100 mV (Figure 2f), as illustrated in Figure 5b. Under short-wavelength LED illumination, the incident photons excite electrons to the defect states in the ZnO layer (Figure 5c). Some of the trapped electrons can be collected by the underlying AgNW networks, and others may inhibit the transfer of electrons from MoS_2 to ZnO. The valence band holes in the ZnO layer can be transferred to the MoS_2 flake.

In addition to the processes above, the AgNW-induced potential modifications affect the charge redistribution under light illumination, as depicted in Figure 5d. Under light illumination, the CPD contrast in Figure 2c becomes less, as also observed in the CPD_L profiles in Figure 2d. This indicates that the light-induced CPD changes are driven not only by charge transfer across the MoS_2/ZnO interface but also by charge drift caused by the potential gradient at the MoS_2 surface. Photogenerated electrons and holes migrate toward regions with higher and lower CPD, respectively. The increased density of negatively charged electrons (or positively charged holes) reduces (or increases) the local CPD. As a result, light illumination leads to a reduction in CPD contrast. The reduced CPD contrast under illumination provides experimental evidence of charge drift in the MoS_2/ZnO-AgNW heterojunction. The combined effect of these processes determines the magnitude and polarity of the SPV signals measured at the MoS_2/ZnO-AgNW surface, as illustrated in Figure 5d.

For optical investigation of the interfacial CT processes, the photoluminescence (PL) measurements of MoS_2/ZnO and MoS_2/ZnO-AgNW were performed, as shown in **Figure 6**a–f. The relatively large PL intensity regions in Figure 6a,c correspond to the 1L-MoS_2 flake regions. Uniform PL intensities (Figure 6a,c) and peak positions (Figure 6b,d) indicate the fabrication of homogeneous heterojunctions. Figure 6e,f show that the largest PL peaks appear near 680 nm, indicating the successful preparation of 1L-MoS_2 flakes.[5–7] The PL spectra of the samples with and without the embedded AgNWs showed that, under 532-nm excitation, the PL emission primarily originates from the MoS_2 flakes in the heterojunctions (Figure S9, Supporting

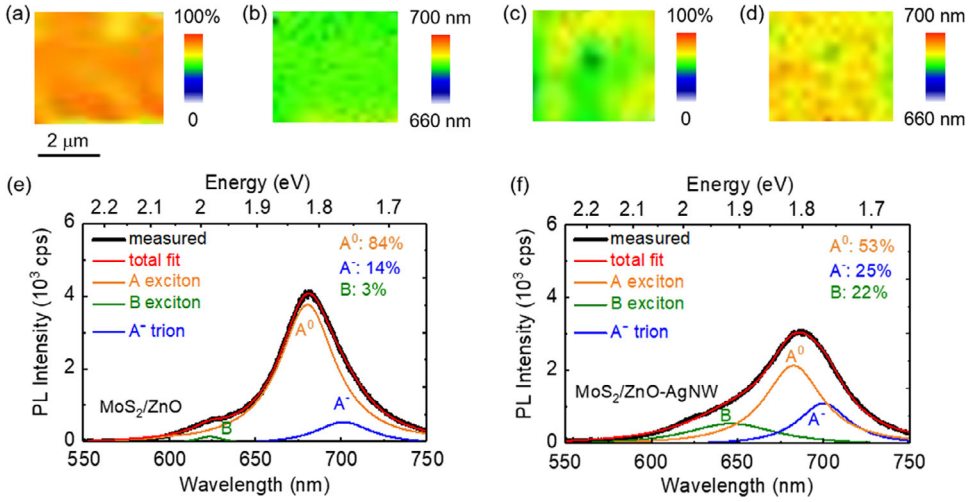


Figure 6. PL intensity maps a,c) and PL peak wavelength maps b,d) of 1L-MoS_2/ZnO and 1L-MoS_2/ZnO-AgNW. The PL intensities are normalized to the maximum value of the 1L-MoS_2/ZnO sample. PL spectra of e) 1L-MoS_2/ZnO and f) 1L-MoS_2/ZnO-AgNW.

© 2025 The Author(s). Advanced Electronic Materials published by Wiley-VCH GmbH

2199160x, 2025, 6, Downloaded from https://advanced.onlinelibrary.wiley.com/doi/10.1002/aelm.202400744 by Ewha Womans University Library, Wiley Online Library on [10/08/2025]. See the Terms and Conditions (https://onlinelibrary.wiley.com/terms-and-conditions) on Wiley Online Library for rules of use; OA articles are governed by the applicable Creative Commons License

Information). Since the spatial resolution (≈0.5 μm) of our PL system is limited, the AgNW-induced inhomogeneous strain states cannot be revealed in the PL maps.

Note that 1L-MoS_2/ZnO-AgNW has a lower overall PL intensity than 1L-MoS_2/ZnO. In general, three primary mechanisms affect the PL characteristics of metal-semiconductor hybrid nanostructures: 1) plasmon-mediated scattering can enhance emission, while plasmon-related absorption can suppress it; 2) local field enhancement increases the excitation rate and radiative recombination rate; and 3) electron transfer from metals to semiconductors can enhance PL while electron transfer from semiconductors to metals results in PL quenching.[29] Since the enhancement and quenching processes compete with one another, systems containing metal nanostructures may not always exhibit enhanced PL intensity. As discussed above, the AgNW-induced local strain in the MoS_2 flakes should be considered for our MoS_2/ZnO-AgNW heterojunctions. The strain at the MoS_2/ZnO interface can reduce the interfacial barrier height, and the resulting efficient electron transfer from MoS_2 to ZnO can decrease the PL intensity.[15] Moreover, the AgNW networks improve the electrical conductivity of the ZnO layers. Therefore, the CT process at the MoS_2/ZnO interface can be enhanced in MoS_2/ZnO-AgNW when compared to MoS_2/ZnO. The suppressed radiative recombination from the MoS_2 flake in MoS_2/ZnO-AgNW indicates the efficient dissociation and transport of the photogenerated charge carriers at the MoS_2/ZnO heterointerface.

It is noteworthy that the PL spectrum of MoS_2/ZnO-AgNW (Figure 6f) is more asymmetric compared to that of MoS_2/ZnO (Figure 6e), suggesting an increase in the emission of high-order excitons and trions.[5,7] For detailed analysis, the spectra were deconvoluted into distinct peaks representing A neutral (A^0), A trion (A^-), and B exciton (B) emissions using Lorentzian fittings. The intense peaks at 680 and 684 nm observed in 1L-MoS_2 on ZnO and ZnO-AgNW, respectively, can be attributed to A^0 excitons. The redshift in the A^0 exciton emission may originate from the aforementioned tensile strain induced by AgNWs. Based on an earlier report,[5] the strain estimated from the PL peak shift can be as large as 1.4%, which is consistent with that estimated from the Raman peak shift (Figure 1c). The relative trion contribution (A^-) in the PL spectrum of MoS_2/ZnO-AgNW (25%) is two times larger than that of MoS_2/ZnO (13%). As depicted in Figure 5d, the following processes likely influence the spatial distribution of the charges in MoS_2/ZnO-AgNW: charge transfer across the MoS_2/ZnO interface, transfer of the trapped electrons from the ZnO layer to AgNWs, and the potential-gradient-driven charge drift. The combined effects of these processes impact the light emission characteristics of MoS_2 flakes, particularly in regions near the AgNWs, resulting in the distinct spectral features observed in Figure 6e,f.

The A^0 and B exciton contributions in MoS_2/ZnO are estimated to be 84% and 3%, respectively, consistent with previous reports.[5,7] In contrast, MoS_2/ZnO-AgNW exhibits a significantly higher B exciton emission (22%) compared to the A^0 exciton emission (53%). McCreary et al. reported that the effective A^0 exciton lifetime (≈10 ps) is much longer than the effective B exciton lifetime (≈1 ps).[7] Based on such distinction, they suggested that non-radiative recombination processes occurring within 10 ps could substantially reduce A exciton emission in samples with high defect densities. The non-flat ZnO-AgNW surface could impose highly localized strain and create structural defects in the MoS_2 flake, as suggested by the broad Raman mode peaks (Figure 1c). These defects are likely responsible for the high density of non-radiative recombination sites, decreasing overall PL intensity and altering the A-to-B exciton emission ratio.

3. Conclusion

In this study, large-area monolayer MoS_2 flakes, prepared via metal-assisted exfoliation, are transferred onto AgNW-embedded ZnO thin films. The measured SPV of the MoS_2/ZnO heterojunctions with AgNWs is ≈200 mV, which is much larger than the SPV of the heterojunctions without AgNWs (≈50 mV). Notably, optical calculations reveal that AgNWs possess a broadband light-concentrating capability, extending well beyond the plasmonic resonance wavelength range. Furthermore, AgNW-induced electric potential modifications at the MoS_2 surface drive the efficient separation of photogenerated excitons and promote the drift of charge carriers. As a result, the highly conducting AgNWs significantly enhance the collection of photogenerated charge carriers. These synergistic optical and electrical benefits of AgNWs enable highly efficient charge transfer at the MoS_2/ZnO heterointerfaces. This work highlights the integration of AgNWs with MoS_2/ZnO heterojunctions as a versatile platform for novel TMD-based optoelectronic applications.

4. Experimental Section

Raman and Photoluminescence Measurements: The optical properties of the samples were characterized using a micro Raman and photoluminescence (PL) system (XperRam, Nanobase) based on an optical microscope (BX43, Olympus). A 532 nm laser (Cobolt 08-DPL) with a power output of 1 mW was focused using a 40 × objective lens with a numerical aperture of 0.75 (MplanFLN, Olympus). Gratings with 1800 and 600 lines mm^{-1} were used for Raman and PL measurements, respectively. PL mapping was performed with a spatial resolution of 0.5 μm and an acquisition time of 500 ms per point.

Scanning Probe Microscopy Measurements: The surface morphology and the local contact potential difference (CPD) of the samples were simultaneously acquired using an atomic force microscopy (AFM) system (NX-10, Park Systems) in a glove box.[21,28] All the measurements were carried out in an N_2 atmosphere to avoid artifacts due to ambient gas adsorption.[21] Pt/Ir-coated Si cantilevers (NSG01Pt, NT-MDT) were used as the probes, and their work functions were calibrated against a highly ordered pyrolytic graphite (HOPG, SPI Suppliers) reference sample. In the amplitude-modulation Kelvin probe force microscopy (KPFM) mode, an AC voltage of 2 V at a frequency of 17 kHz was applied to the probes. The illumination intensity of the LEDs was measured using a photodiode power sensor (S170C, Thorlabs).

Finite-Difference Time-Domain (FDTD) Calculations: Numerical calculations were performed using commercial FDTD software (Lumerical FDTD Solutions, Ansys). The optical constants of glass,[32] Ag,[32] and ZnO,[33] were obtained from the literature. A plane wave source was positioned 0.9 μm above the ZnO surface, and the simulations were conducted across wavelengths ranging from 300 to 800 nm with a mesh size of 2.0 × 2.0 × 2.0 nm^3. Perfectly matched layer boundary conditions were applied at the simulation box boundaries in the out-of-plane direction, while Bloch boundary conditions were used in the in-plane directions.

© 2025 The Author(s). Advanced Electronic Materials published by Wiley-VCH GmbH

2199160x, 2025, 6, Downloaded from https://advanced.onlinelibrary.wiley.com/doi/10.1002/aelm.202400744 by Ewha Womans University Library, Wiley Online Library on [10/08/2025]. See the Terms and Conditions (https://onlinelibrary.wiley.com/terms-and-conditions) on Wiley Online Library for rules of use; OA articles are governed by the applicable Creative Commons License

Supporting Information

Supporting Information is available from the Wiley Online Library or from the author.

Acknowledgements

This work was supported by the National Research Foundation of Korea Grants (NRF- RS-2022-NR070782, RS-2024-00341837, RS-2024-00406827, and RS-2024-0034883) funded by the Ministry of Science and ICT of the Korea Government.

Conflict of Interest

The authors declare no conflict of interest.

Data Availability Statement

The data that support the findings of this study are available from the corresponding author upon reasonable request.

Keywords

Ag nanowire, charge transfer, heterojunction, MoS_2, surface photovoltage, ZnO

Received: September 24, 2024
Revised: February 26, 2025
Published online: March 18, 2025

[1] E. C. Regan, D. Wang, E. Y. Paik, Y. Zeng, L. Zhang, J. Zhu, A. H. MacDonald, H. Deng, F. Wang, *Nat. Rev. Mater.* **2022**, *7*, 778.
[2] L. Huang, A. Krasnok, A. Alu, Y. Yu, D. Neshev, A. E. Miroshnichenko, *Rep. Prog. Phys.* **2022**, *85*, 046401.
[3] M. Bernadi, M. Palummo, J. C. Grossman, *Nano Lett.* **2013**, *13*, 3664.
[4] S. E. Panasci, E. Schiliro, G. Greco, M. Cannas, F. M. Gelardi, S. Agnello, F. Roccaforte, F. Giannazzo, *ACS Appl. Mater. Interfaces* **2021**, *13*, 31248.
[5] S. Golovynskyi, O. I. Datsenko, A. I. Pérez-Jiménez, A. Kuklin, M. Chaigneau, A. Golovynskyi, I. Golovynska, M. Bosi, L. Seravalli, *ACS Appl. Nano Mater.* **2024**, *7*, 15570.
[6] A. Castellanos-Gomez, R. Roldán, E. Cappelluti, M. Buscema, F. Guinea, H. S. J. van der Zant, G. A. Steel, *Nano Lett.* **2013**, *13*, 5361.
[7] K. M. McCreary, A. T. Hanbicki, S. V. Sivaram, B. T. Jonker, *APL Mater.* **2018**, *6*, 111106.
[8] A. Castellanos-Gomez, M. Buscema, R. Molenaar, V. Singh, L. Janssen, H. S. J. van der Zant, G. A. Steele, *2D Mater.* **2014**, *1*, 011002.
[9] L. Pirker, J. Honolka, M. Velický, O. Frank, *2D Mater.* **2024**, *11*, 022003.
[10] A. T. Nguyen, J. Wang, E. Cho, S. Lim, S. Kwon, J. Song, K. Zhou, D.-W. Kim, *Adv. Mater. Interfaces* **2023**, *10*, 2300031.
[11] S. Moon, A. T. Nguyen, J. Cho, J. Song, E. Cho, S. Lim, C.-H. Cho, D.-W. Kim, *J. Alloys Compd.* **2024**, *1002*, 175241.
[12] A. T. Alanazi, A. Alotaibi, M. Alqahtani, J. H. Rice, *ACS Omega* **2023**, *8*, 6318.
[13] X. Zhu, W. Liu, C. Sheng, C. Cong, X. Chen, H. Tang, Y. Luo, S. Li, J. Chu, R. Zhang, *ACS Appl. Mater. Interfaces* **2024**, *16*, 15446.
[14] M. S. Kim, S. Roy, J. Lee, B. G. Kim, H. Kim, J.-H. Park, S. J. Yun, G. H. Han, J.-Y. Leem, J. Kim, *ACS Appl. Mater. Interfaces* **2016**, *8*, 28809.
[15] B. Liu, Q. Liao, X. Zhang, J. Du, Y. Ou, J. Xiao, Z. Kang, Z. Zhang, Y. Zhang, *ACS Nano* **2019**, *13*, 9057.
[16] M.-A. Kang, S. Kim, I.-S. Jeon, Y. R. Lim, C.-Y. Park, W. Song, S. S. Lee, J. Lim, K.-S. An, S. Myung, *RSC Adv.* **2019**, *9*, 19707.
[17] C. H. Jiang, C. B. Yao, Z. M. Wang, X. Wang, L. Y. Wang, T. T. Chen, S. B. Yang, *J. Alloys Compd.* **2022**, *912*, 165183.
[18] J. Jang, Y. Kim, S. S. Chee, H. Kim, D. Whang, G. H. Kim, S. J. Yun, *ACS Appl. Mater. Interfaces* **2020**, *12*, 5031.
[19] J. Shi, J. Zhang, L. Yang, M. Qu, D.-C. Qi, K. H. L. Zhang, *Adv. Mater.* **2021**, *33*, 2006230.
[20] M. Patel, S. Ghosh, J. E. Park, J. Song, D.-W. Kim, J. Kim, *J. Mater. Chem. C* **2023**, *11*, 14559.
[21] J. Song, M. Patel, S. E. Johannesson, K. Cho, J. H. Park, J. Kim, D.-W. Kim, *Adv. Electron. Mater.* **2023**, *9*, 230036.
[22] H. H. Khaligh, L. Xu, A. Khosropour, A. Madeira, M. Romano, C. Pradére, M. Tréguer-Delapierre, L. Servant, M. A. Pope, I. A. Goldthorpe, *Nanotechnology* **2017**, *28*, 425703.
[23] V. H. Nguyen, D. T. Papanastasiou, J. Resende, L. Bardet, T. Sannicolo, C. Jiménez, D. Muñoz-Rojas, N. D. Nguyen, D. Bellet, *Small* **2022**, *18*, 2106006.
[24] I. Ibrahim Zamkoye, J. Bouclé, N. Leclerc, B. Lucas, S. Vedraine, *Sol. RRL* **2023**, *7*, 2200756.
[25] A. Moussa, Bogdanowicz, B. Groven, P. Morin, M. Beggiato, M. Saib, G. Santoro, Y. Abramovitz, K. Houchens, S. Ben Nissim, *Jpn. J. Appl. Phys.* **2024**, *63*, 030802.
[26] S. Kronik, Y. Shapira, *Surf. Sci. Rep.* **1999**, *37*, 1.
[27] V. Donchev, *Mater. Res. Express* **2019**, *6*, 103001.
[28] A. Sohn, H. Moon, J. Kim, M. Seo, K.-A. Min, S. W. Lee, S. Yoon, S. Hong, D.-W. Kim, *J. Phys. Chem. C* **2017**, *121*, 22517.
[29] X. D. Zhou, X. H. Xiao, J. X. Xu, G. X. Cai, F. Ren, C. Z. Jiang, *EPL* **2011**, *93*, 57009.
[30] J. Cao, T. Sun, K. T. V. Grattan, *Sens. Act. B* **2014**, *195*, 332.
[31] Y. Liu, X. Zhang, J. Su, H. Li, Q. Zhang, Y. Gao, *Opt. Express* **2014**, *24*, 30148.
[32] E. D. Palik, *Handbook of optical constants of solids*, Academic Press, San Diego, CA **1985**.
[33] O. Aguilar, S. de Castro, M. P. F. Godoy, M. Rebello Sousa Dias, *Opt. Mater. Express* **2019**, *9*, 3638.

© 2025 The Author(s). Advanced Electronic Materials published by Wiley-VCH GmbH

2199160x, 2025, 6, Downloaded from https://advanced.onlinelibrary.wiley.com/doi/10.1002/aelm.202400744 by Ewha Womans University Library, Wiley Online Library on [10/08/2025]. See the Terms and Conditions (https://onlinelibrary.wiley.com/terms-and-conditions) on Wiley Online Library for rules of use; OA articles are governed by the applicable Creative Commons License